Searches for exclusive Higgs and Z boson decays into $J/\psi\,\gamma$, $\psi(2S)\,\gamma$, and $\Upsilon(nS)\,\gamma$ at $\sqrt{s} = 13$ TeV with the ATLAS detector

The ATLAS Collaboration *

A B S T R A C T

Searches for the exclusive decays of the Higgs and Z bosons into a J/ψ, $\psi(2S)$, or $\Upsilon(nS)$ $(n = 1, 2, 3)$ meson and a photon are performed with a pp collision data sample corresponding to an integrated luminosity of 36.1 fb^{-1} collected at $\sqrt{s} = 13$ TeV with the ATLAS detector at the CERN Large Hadron Collider. No significant excess of events is observed above the expected backgrounds, and 95% confidence-level upper limits on the branching fractions of the Higgs boson decays to $J/\psi\,\gamma$, $\psi(2S)\,\gamma$, and $\Upsilon(nS)\,\gamma$ of 3.5×10^{-4}, 2.0×10^{-3}, and $(4.9, 5.9, 5.7) \times 10^{-4}$, respectively, are obtained assuming Standard Model production. The corresponding 95% confidence-level upper limits for the branching fractions of the Z boson decays are 2.3×10^{-6}, 4.5×10^{-6} and $(2.8, 1.7, 4.8) \times 10^{-6}$, respectively.

1. Introduction

Following the observation of a Higgs boson H with a mass of approximately 125 GeV by the ATLAS and CMS collaborations [1,2], detailed measurements of its properties show no deviations from the Standard Model (SM) [3]. However, its role in fermion mass generation is still to be shown experimentally. In the SM, this mass generation is implemented through Yukawa interactions, and many theories beyond the SM predict substantial modifications of the relevant Higgs boson couplings to fermions. The ATLAS and CMS collaborations have reported measurements of the Higgs coupling to a third-generation fermion with a significance greater than five standard deviations in the $H \to \tau^+\tau^-$ channel [3–5]. In addition, progress has been made in the third-generation quark sector with indirect evidence of the coupling of the Higgs boson to the top quark [3]. This was recently complemented by direct observation of the associated production of the Higgs boson with a top-quark pair ($t\bar{t}H$) [6,7]. Evidence of Higgs boson decays into $b\bar{b}$ has also been found with a significance in excess of three standard deviations by both ATLAS and CMS [8–10]. No experimental evidence of Higgs boson decays into the first- and second-generation fermions has yet been found, but direct searches were recently performed by the ATLAS Collaboration for $H \to c\bar{c}$ [11] and $H \to \mu^+\mu^-$ [12, 13] and by the CMS Collaboration for $H \to \mu^+\mu^-$ and $H \to e^+e^-$ decays [14].

The Standard Model Higgs boson decays $H \to J/\psi\,\gamma$ and $H \to \psi(2S)\,\gamma$ offer an opportunity to access the c-quark Yukawa

coupling [15,16] in a manner complementary to studies of the inclusive decay $H \to c\bar{c}$. The branching fraction for $H \to J/\psi\,\gamma$ has been calculated within the SM to be $\mathcal{B}(H \to J/\psi\,\gamma) = (2.99^{+0.16}_{-0.15}) \times 10^{-6}$ [17]. Other recent results on these calculations are given in Refs. [18–20]. For $H \to \psi(2S)\,\gamma$ the branching fraction was calculated by the authors of Ref. [17] to be $\mathcal{B}(H \to \psi(2S)\,\gamma) = (1.03 \pm 0.06) \times 10^{-6}$ using an estimate for the value of the order-v^2 NRQCD long-distance matrix element.

The corresponding decays in the bottomonium sector, $H \to \Upsilon(1S, 2S, 3S)\,\gamma$, can provide, in combination with $H \to b\bar{b}$ decays, information about the real and imaginary parts of the b-quark coupling to the Higgs boson [19], which could probe potential CP violation in the Higgs sector. However, the expected SM branching fractions, $\mathcal{B}(H \to \Upsilon(nS)\,\gamma) = (5.22^{+2.02}_{-1.70}, 1.42^{+0.72}_{-0.57}, 0.91^{+0.48}_{-0.38}) \times 10^{-9}$ $(n = 1, 2, 3)$ [17,18], are smaller due to a cancellation between the "direct" and "indirect" amplitudes. The direct amplitude proceeds through the $H \to q\bar{q}$ coupling with a subsequent photon emission before the $q\bar{q}$ hadronisation to $\Upsilon(nS)$. The indirect amplitude proceeds via the $H\gamma\gamma$ coupling followed by the fragmentation $\gamma^* \to \Upsilon(nS)$.

Deviations of the c- and b-quark Yukawa couplings from the SM expectations can lead to significant increases in the branching fractions for exclusive decays. These deviations can arise in beyond-the-SM theories; for example, the quark masses might not originate entirely from the Higgs mechanism but could also be induced by other subdominant sources of electroweak symmetry breaking [21]. Other scenarios include the minimal flavour violation framework [22], the Froggatt–Nielsen mechanism [23], the Higgs-dependent Yukawa couplings model [24], the Randall–Sundrum family of models [25], and the possibility of the Higgs boson being

* *E-mail address:* atlas.publications@cern.ch.

a composite pseudo-Goldstone boson [26]. An overview of relevant models of physics beyond-the-SM is provided in Ref. [27].

Decays of the Higgs boson into a heavy, vector quarkonium state, $\mathcal{Q} \equiv J/\psi$ or $\Upsilon(nS)$, and a photon were searched for by the ATLAS Collaboration with up to 19.2 fb^{-1} of data collected at $\sqrt{s} = 8$ TeV [28], resulting in 95% confidence level (CL) upper limits of 1.5×10^{-3} for $\mathcal{B}(H \to J/\psi\,\gamma)$ and $(1.3, 1.9, 1.3) \times 10^{-3}$ for $\mathcal{B}(H \to \Upsilon(nS)\,\gamma)$ ($n = 1, 2, 3$). The former decay mode was also searched for by the CMS Collaboration [29], yielding a similar upper limit. In addition, the ATLAS Collaboration searched for the rare Higgs decays $H \to \phi\,\gamma$ and $H \to \rho\,\gamma$ [30,31].

Owing to the large Z boson production cross section at the LHC, rare Z boson decays can be probed at much lower rates than for Higgs boson decays into the same final state. Branching fractions for $Z \to \mathcal{Q}\,\gamma$ decays have been calculated to be between 10^{-8} and 10^{-7} for both the $Z \to J/\psi\,\gamma$ and $Z \to \Upsilon(nS)\,\gamma$ decays [32–34]. Measurements of the branching fractions for these decays would provide a sensitive test of the SM and the factorisation approach in quantum chromodynamics (QCD), since the power corrections in terms of the ratio of the QCD energy scale to the vector-boson mass are small [33]. ATLAS searched for Z boson decays into J/ψ or $\Upsilon(nS)$ ($n = 1, 2, 3$) and a photon with 20.3 fb^{-1} of data collected at $\sqrt{s} = 8$ TeV [28], resulting in 95% CL upper limits of 2.6×10^{-6} and $(3.4, 6.5, 5.4) \times 10^{-6}$, respectively. ATLAS also searched for the decay modes $Z \to \phi\,\gamma$ and $Z \to \rho\,\gamma$ [30,31].

This Letter describes searches for Higgs and Z boson decays into the exclusive final states $J/\psi\,\gamma$, $\psi(2S)\,\gamma$, and $\Upsilon(nS)\,\gamma$ ($n = 1, 2, 3$) with $J/\psi \to \mu^+\mu^-$, $\psi(2S) \to \mu^+\mu^-$, and $\Upsilon(nS) \to \mu^+\mu^-$ using ATLAS data collected in 2015 and 2016 at $\sqrt{s} = 13$ TeV. Throughout the remainder of this Letter, where no distinction is relevant, the J/ψ and $\psi(2S)$ states are referred to collectively as the $\psi(nS)$ states.

2. ATLAS detector

ATLAS [35] is a multipurpose particle detector with a forward–backward symmetric cylindrical geometry and near 4π coverage in solid angle.[1] It consists of an inner tracking detector, electromagnetic and hadronic calorimeters, and a muon spectrometer.

The inner tracking detector (ID) covers the pseudorapidity range $|\eta| < 2.5$ and is surrounded by a thin superconducting solenoid providing a 2 T magnetic field. At small radii, a high-granularity silicon pixel detector surrounds the vertex region and typically provides four measurements per track. It is followed by a silicon microstrip tracker, which provides eight measurement points per track. The silicon detectors are complemented by a gas-filled straw-tube transition radiation tracker, which enables radially extended track reconstruction up to $|\eta| = 2.0$ with typically 35 measurements per track.

Electromagnetic (EM) calorimetry within the region $|\eta| < 3.2$ is provided by barrel and endcap high-granularity lead/liquid-argon (LAr) EM calorimeters with an additional thin LAr presampler covering $|\eta| < 1.8$ to correct for energy loss in upstream material; for $|\eta| < 2.5$ the EM calorimeter is divided into three layers in depth. A steel/scintillator-tile calorimeter provides hadronic calorimetry for $|\eta| < 1.7$. LAr technology with copper as absorber is used for the hadronic calorimeters in the endcap region $1.5 < |\eta| < 3.2$. The solid-angle coverage is completed with forward copper/LAr and

tungsten/LAr calorimeter modules in $3.1 < |\eta| < 4.9$ optimised for EM and hadronic measurements, respectively.

The muon spectrometer surrounds the calorimeters and has separate trigger and high-precision tracking chambers measuring the deflection of muons in a magnetic field provided by three air-core superconducting toroidal magnets. The precision chamber system covers the region $|\eta| < 2.7$ with three layers of monitored drift tubes, complemented by cathode strip chambers in the forward region. The muon trigger system covers the range $|\eta| < 2.4$ with resistive plate chambers in the barrel and thin gap chambers in the endcap regions.

A two-level trigger and data acquisition system is used to record events for offline analysis [36]. The level-1 trigger is implemented in hardware and uses a subset of detector information to reduce the event rate to at most 100 kHz. It is followed by a software-based high-level trigger which filters events using the full detector information and outputs events for permanent storage at an average rate of 1 kHz.

3. Data and simulated data

The search is performed with a sample of pp collision data recorded at a centre-of-mass energy $\sqrt{s} = 13$ TeV corresponding to an integrated luminosity of 36.1 fb^{-1}. The integrated luminosity of the data sample has an uncertainty of 2.1% derived using the method described in Ref. [37]. Events are retained for further analysis only if they were collected under stable LHC beam conditions and all relevant detector components were fully functional.

The data samples used in this analysis were collected by a combination of two triggers [36]. The first required an isolated photon with transverse momentum p_T^γ greater than 35 GeV and at least one muon with p_T^μ greater than 18 GeV. The second required an isolated photon with $p_T^\gamma > 25$ GeV and a muon with $p_T^\mu > 24$ GeV. The use of two triggers with differing transverse momentum thresholds on the photon and muon objects offers an increased trigger efficiency with respect to the case of either trigger used alone.

Higgs boson production was modelled using the Powheg-Box v2 Monte Carlo (MC) event generator [38–42] with CT10 parton distribution functions [43] for the gluon–gluon fusion (ggH) and vector-boson fusion (VBF) processes. Both processes were calculated up to next-to-leading order (NLO) in α_S. Powheg-Box was interfaced with Pythia 8.186 [44,45] to model the parton shower, hadronisation, and underlying event with the AZNLO set of tuned parameters [46]. Additional contributions from the associated production of a Higgs boson and a W or Z boson (denoted WH and ZH, respectively) were modelled by the Pythia 8.186 event generator [44,45] with NNPDF23LO parton distribution functions [47] and the A14 set of tuned parameters for hadronisation and the underlying event [48]. The production rates for the SM Higgs boson with $m_H = 125$ GeV, obtained from the compilation in Ref. [27], are assumed throughout this analysis. The ggH production is normalised such that it reproduces the total cross section predicted by a next-to-next-to-next-to-leading-order QCD calculation with NLO electroweak corrections applied [49–52]. The VBF production is normalised to an approximate next-to-next-to-leading-order (NNLO) QCD cross section with NLO electroweak corrections applied [53–55]. The production of WH and ZH is normalised to cross sections calculated at NNLO in QCD with NLO electroweak corrections [56,57] including the NLO QCD corrections [58] for $gg \to ZH$. The production of a Higgs boson in association with $t\bar{t}$ ($t\bar{t}H$) or $b\bar{b}$ ($b\bar{b}H$) is accounted for by scaling the total cross section used to normalise the ggH signal sample, assuming the signal efficiency of these processes to be equal to that for ggH. The ad-

---

[1] ATLAS uses a right-handed coordinate system with its origin at the nominal interaction point (IP) in the centre of the detector and the z-axis along the beam pipe. The x-axis points from the IP to the centre of the LHC ring, and the y-axis points upward. Cylindrical coordinates (r, ϕ) are used in the transverse plane, ϕ being the azimuthal angle around the z-axis. The pseudorapidity is defined in terms of the polar angle θ as $\eta = -\ln\tan(\theta/2)$.

dition of $t\bar{t}H$ and $b\bar{b}H$ to the ggH signal changes the acceptance by less than 1%.

The Powheg-Box v2 event generator was also used to model inclusive Z boson production. Pythia 8.186 [44,45] with CTEQ6L1 parton distribution functions [59] and the AZNLO set of hadronisation and underlying-event parameters [46] was used to simulate parton showering and hadronisation. The prediction is normalised to the total cross section obtained from the measurement in Ref. [60], which has an uncertainty of 2.9%. This conservatively assumes the luminosity component of the uncertainty to be completely uncorrelated with that of this search.

The Higgs and Z boson decays were simulated as a cascade of two-body decays, accounting for effects of the quarkonium helicity on the $\mu^+\mu^-$ kinematics. The quarkonium state is simulated to be transversely polarised in the case of the Higgs boson decay and longitudinally polarised in the case of the Z boson decay [34]. The branching fractions for the decays $\mathcal{Q} \to \mu^+\mu^-$ are taken from Ref. [61]. The simulated events were passed through the detailed Geant 4 simulation of the ATLAS detector [62,63] and processed with the same software used to reconstruct the data.

4. Event selection for $\psi(nS)\gamma \to \mu^+\mu^-\gamma$ and $\Upsilon(nS)\gamma \to \mu^+\mu^-\gamma$

Muons are reconstructed from ID tracks combined with independent muon spectrometer tracks or track segments [64] and are required to have $p_T^\mu > 3$ GeV and pseudorapidity $|\eta^\mu| < 2.5$. Candidate $\mathcal{Q} \to \mu^+\mu^-$ decays are reconstructed from pairs of oppositely charged muons consistent with originating from a common vertex. The highest-p_T muon in a pair, called the leading muon in the following, is required to have $p_T^\mu > 18$ GeV. Dimuons with a mass $m_{\mu^+\mu^-}$ within $2.0 < m_{\mu^+\mu^-} < 4.2$ GeV are identified as $\psi(nS) \to \mu^+\mu^-$ candidates. Dimuons with $8.0 < m_{\mu^+\mu^-} < 12.0$ GeV are considered to be $\Upsilon(nS) \to \mu^+\mu^-$ candidates.

Selected $\mathcal{Q} \to \mu^+\mu^-$ candidates are subjected to isolation and vertex-quality requirements. In this case, the primary pp vertex is defined as the reconstructed vertex with the highest $\Sigma_i p_{T_i}^2$ of all associated tracks used to form the vertex. The sum of the p_T of the tracks within $\Delta R = \sqrt{(\Delta\phi)^2 + (\Delta\eta)^2} = 10$ GeV/p_T^μ (with a maximum ΔR of 0.3) of the leading muon is required to be less than 6% of the muon p_T [65]. To mitigate the effects of multiple pp interactions in the same or neighbouring bunch crossings, only ID tracks that originate from the primary vertex are considered. The transverse momentum of the ID track associated with the leading muon is subtracted from the sum, and the subleading muon is also subtracted if it falls within the isolation cone. To reject backgrounds from b-hadron decays, the signed projection of the $\mathcal{Q}$ candidate's flight distance between the primary pp vertex and the dimuon vertex onto the direction of its transverse momentum is required to be less than three times its uncertainty.

Photons are reconstructed from clusters of energy in the electromagnetic calorimeter. Clusters without matching ID tracks are classified as unconverted photon candidates while clusters matched to ID tracks consistent with the hypothesis of a photon conversion into e^+e^- are classified as converted photon candidates [66]. Reconstructed photon candidates are required to have transverse momentum $p_T^\gamma > 35$ GeV and pseudorapidity $|\eta^\gamma| < 2.37$, excluding the barrel/endcap calorimeter transition region $1.37 < |\eta^\gamma| < 1.52$, and to satisfy the "tight" photon identification criteria [66]. Isolation requirements are imposed to further suppress the contamination from jets. The sum of the transverse momenta of all tracks originating from the primary vertex, within $\Delta R = 0.2$ of the photon direction, excluding those associated with reconstructed photon conversions, is required to be less than 5% of p_T^γ. In addition to this track isolation criterion, a calorime-

ter isolation criterion is applied where the sum of the transverse momenta of calorimeter energy clusters within $\Delta R = 0.4$ of the photon direction, excluding the transverse energy of the reconstructed photon, is required to be less than $\left(2.45 \text{ GeV} + 0.022 p_T^\gamma\right)$. The effects of multiple pp interactions in the events are also accounted for in the calorimeter isolation measurements.

Combinations of a $\mathcal{Q} \to \mu^+\mu^-$ candidate and a photon satisfying $\Delta\phi(\mathcal{Q}, \gamma) > \pi/2$ are retained for further analysis. When multiple combinations are possible, a situation that arises in only a few percent of the events, the combination of the highest-p_T photon and the $\mathcal{Q}$ candidate with an invariant mass closest to the respective quarkonium mass is retained. To improve the sensitivity of the $\Upsilon(nS)\gamma$ analysis in resolving the individual $\Upsilon(nS)$ states, the events are classified into two exclusive categories based upon the pseudorapidity of the muons. Events where both muons are within the region $|\eta^\mu| < 1.05$ constitute the "barrel" (B) category. Events where at least one of the muons is outside the region $|\eta^\mu| < 1.05$ constitute the "endcap" (EC) category.

To maintain a single search region, while ensuring near-optimal sensitivity for both the Higgs and Z boson analyses, the transverse momentum of the $\mathcal{Q}$ candidate $p_T^\mathcal{Q}$ is required to be greater than a value that varies as a function of the invariant mass of the three-body system $m_{\mathcal{Q}\gamma}$. For the $\psi(nS) \to \mu^+\mu^-$ ($\Upsilon(nS) \to \mu^+\mu^-$) selection, $p_T^\mathcal{Q}$ thresholds of 40 GeV (34 GeV) and 54.4 GeV (52.7 GeV) are imposed for the regions $m_{\mathcal{Q}\gamma} \leq 91$ GeV and $m_{\mathcal{Q}\gamma} \geq 140$ GeV, respectively. The thresholds are varied between their minimum and maximum values as a linear function of $m_{\mathcal{Q}\gamma}$ in the region $91 \text{ GeV} < m_{\mathcal{Q}\gamma} < 140$ GeV.

5. Signal modelling

For the $\psi(nS)\gamma \to \mu^+\mu^-\gamma$ final state, the total signal efficiencies (kinematic acceptance, trigger, reconstruction, identification, and isolation efficiencies) are 19% and 11% for the Higgs and Z boson decays, respectively. The corresponding efficiencies for the $\Upsilon(nS)\gamma \to \mu^+\mu^-\gamma$ final states are 22–23% and 15–16%, respectively. The difference in efficiency between the Higgs and Z boson decays arises primarily from the softer p_T^γ and $p_T^{\mu\mu}$ distributions associated with $Z \to \mathcal{Q}\gamma$ production, as seen by comparing Figs. 1(a) and 1(b) for the $J/\psi\gamma$ case and Figs. 1(c) and 1(d) for the $\Upsilon(nS)\gamma$ case.

Accounting for quarkonium helicity effects in the $\mathcal{Q} \to \mu^+\mu^-$ decays leads to a 3–4% decrease of the expected Higgs boson efficiency and a corresponding 6–9% increase of the expected Z boson efficiency, relative to the efficiency for an isotropic decay.

The $m_{\mu^+\mu^-\gamma}$ resolution is 1.6–1.8% for both the Higgs and Z boson decays. For each of the final states, a two-dimensional ($m_{\mu^+\mu^-\gamma}$ and $m_{\mu^+\mu^-}$) probability density function (pdf) is used to model the signal. The Higgs boson signals are modelled with two-dimensional multivariate Gaussian distributions, which retain the correlation between $m_{\mu^+\mu^-\gamma}$ and $m_{\mu^+\mu^-}$ of the final states. For the Z boson decays, the $m_{\mu^+\mu^-\gamma}$ distributions of the signal are modelled with Voigtian pdfs (a convolution of Breit–Wigner and Gaussian pdfs) corrected with mass-dependent efficiency factors, and the $m_{\mu^+\mu^-}$ distributions are modelled as Gaussian pdfs.

The $m_{\mu^+\mu^-}$ distribution for selected $\psi(nS)\gamma$ candidates, which pass the background generation region criteria described in Section 6, is shown in Fig. 2(a) and exhibits clear peaks at the J/ψ and $\psi(2S)$ masses. In Figs. 2(b) and 2(c), the corresponding distributions for the selected $\Upsilon(nS)\gamma$ candidates are shown, where the $\Upsilon(1S, 2S, 3S)$ peaks can be observed. The $\psi(nS)$ and $\Upsilon(nS)$ peaks are fitted with Gaussian pdfs and are used to cross-check the parameters obtained from the fit to simulated signal event samples, while the background is modelled with a Chebychev polynomial function. The experimental resolution in $m_{\mu^+\mu^-}$ is approximately
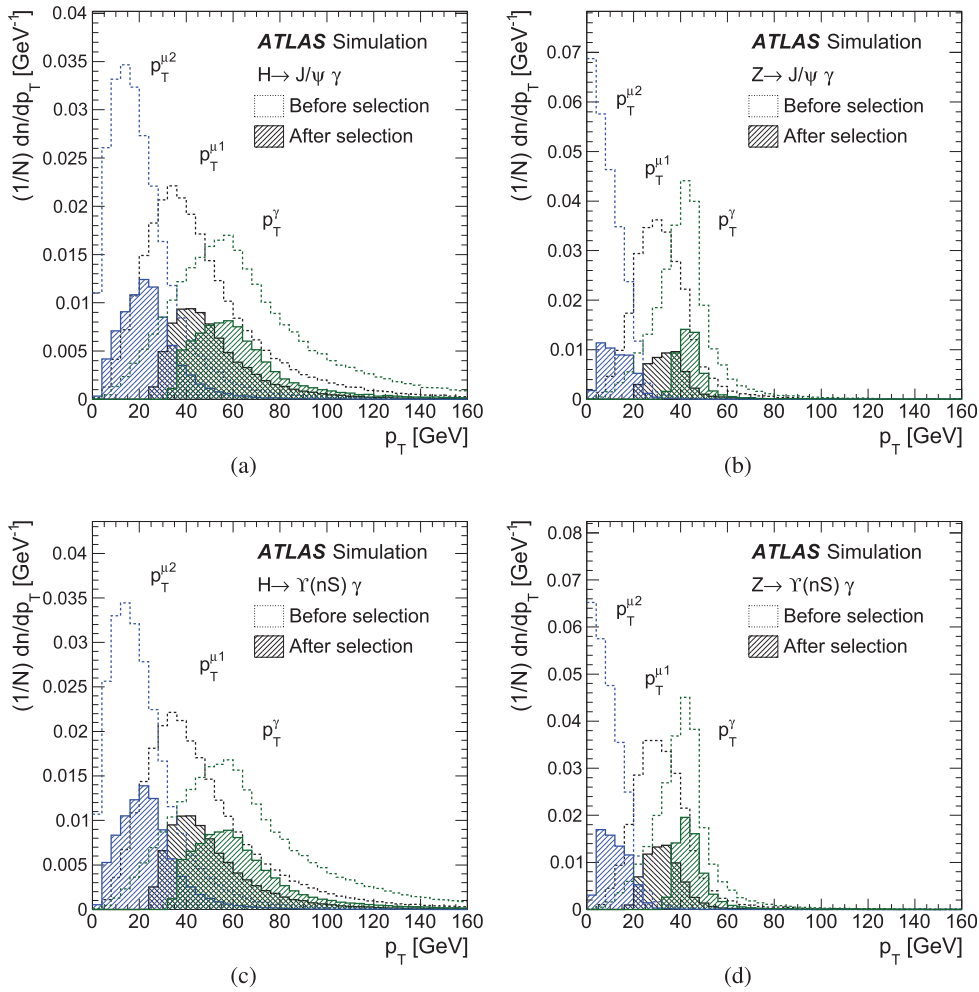
Fig. 1. Generator-level transverse momentum (p_T) distributions of the photon and of the muons, ordered in p_T, for (a) $H \to J/\psi\,\gamma$, (b) $Z \to J/\psi\,\gamma$, (c) $H \to \Upsilon(nS)\,\gamma$ and (d) $Z \to \Upsilon(nS)\,\gamma$ simulated signal events, respectively. The leading muon candidate is denoted by $p_T^{\mu 1}$ and the subleading candidate by $p_T^{\mu 2}$. The hatched histograms denote the full event selection while the dashed histograms show the events at generator level that fall within the analysis geometric acceptance (both muons are required to have $|\eta^\mu| < 2.5$ while the photon is required to have $|\eta^\gamma| < 2.37$, excluding the region $1.37 < |\eta^\gamma| < 1.52$). The dashed histograms are normalised to unity, and the relative difference between the two sets of distributions corresponds to the effects of reconstruction, trigger, and event selection efficiencies.

54 MeV for the $J/\psi\,\gamma$ candidates (43 MeV for events in the barrel category and 64 MeV for events in the endcap category).

6. Background modelling

The dominant source of background exhibits a non-resonant $m_{\mu^+\mu^-\gamma}$ distribution and is composed of two distinct contributions: genuine $\mathcal{Q} \to \mu^+\mu^-$ decays and non-resonant dimuon production. The decay $Z \to \mu^+\mu^-\gamma$ with final-state radiation (Z FSR) constitutes a further, smaller background contribution exhibiting a characteristic resonant structure in the $m_{\mu^+\mu^-\gamma}$ distribution.

The $m_{\mu^+\mu^-\gamma}$ continuum background is modelled with a non-parametric data-driven approach using templates to describe the kinematic distributions. The normalisation of the background is extracted directly from a fit to the data. The shape of the background model in the final discriminant variable is also profiled in the fit. A similar procedure was used in the earlier search for Higgs and Z boson decays into $J/\psi\,\gamma$ and $\Upsilon(nS)\,\gamma$ [28] and the searches for Higgs and Z boson decays into $\phi\,\gamma$ and $\rho\,\gamma$ [30,31].

The background model uses a sample of 5500 $\psi(nS)\,\gamma$ and 2300 $\Upsilon(nS)\,\gamma$ candidate events. These events pass all of the kinematic selection requirements described previously, except that the photon and $\mathcal{Q}$ candidates are not required to satisfy the nominal isolation requirements and a looser minimum $p_T^{\mathcal{Q}}$ requirement of

30 GeV is imposed. These events define the background-dominated "generation region" (GR). From these events, pdfs are constructed to describe the distributions of the relevant kinematic and isolation variables and their most important correlations. The data control samples are corrected for contamination from $Z \to \mu^+\mu^-\gamma$ decays.

The pdfs of these kinematic and isolation variables are sampled to generate an ensemble of pseudocandidates, each with complete $\mathcal{Q}$ and γ four-vectors and the associated $\mathcal{Q}$ and photon isolation values. The important correlations among the kinematic and isolation variables of the background events, in particular between $p_T^{\mathcal{Q}}$ and p_T^{γ}, are retained in the generation of the pseudocandidates through the following sampling scheme:

- Initially, a value for $p_T^{\mathcal{Q}}$ is sampled from the corresponding pdf.
- The distribution of p_T^{γ} is parameterised in bins of $p_T^{\mathcal{Q}}$, and a value is sampled from the corresponding bin given the previously sampled value of $p_T^{\mathcal{Q}}$. The muon isolation variables are parameterised in bins of $p_T^{\mathcal{Q}}$ and p_T^{γ} and sampled according to the previously selected values.
- The distributions of the pseudorapidity difference between $\mathcal{Q}$ and γ, $\Delta\eta(\mathcal{Q}, \gamma)$, the photon calorimeter isolation variable,
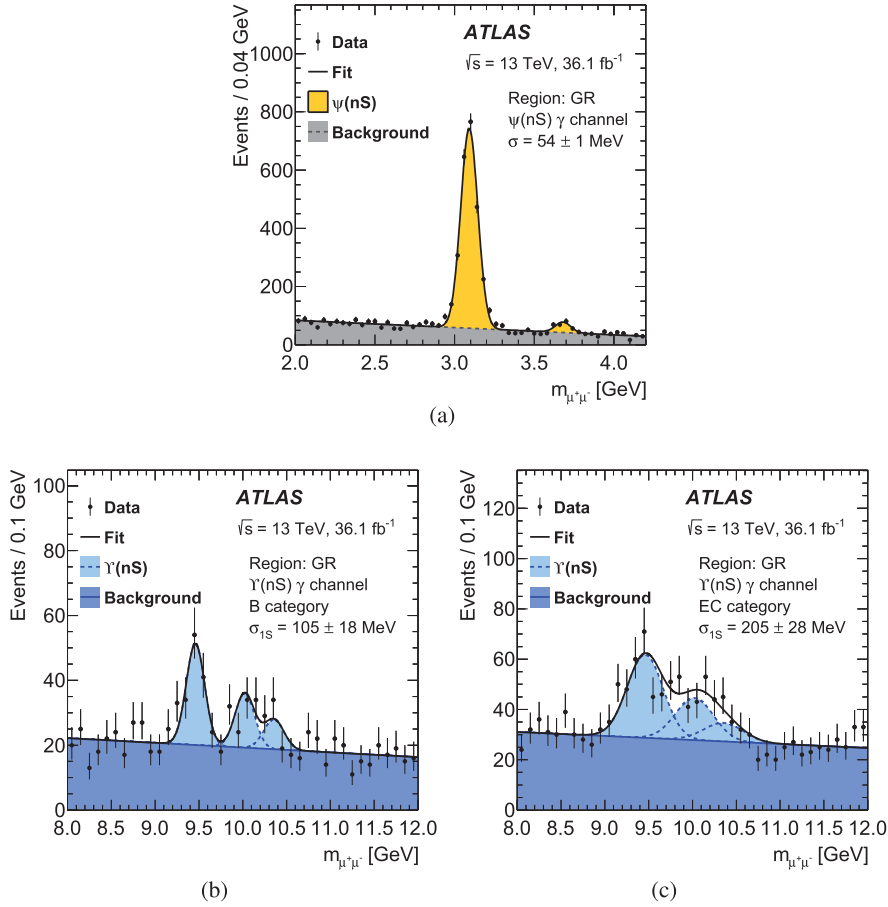
Fig. 2. Distribution of $\mu^+\mu^-$ invariant mass for (a) $\psi(nS)\gamma$ and $\Upsilon(nS)\gamma$ ((b) barrel and (c) endcap categories) candidates. The candidates satisfy the event selection but without the nominal isolation requirements and with a looser minimum $p_T^{\mathcal{Q}}$ requirement of 30 GeV. These events constitute the background "generation region" defined in Section 6.

and their correlations are parameterised in a binned two-dimensional distribution in the same bins of $p_T^{\mathcal{Q}}$ used to describe the p_T^{γ} and muon isolation variables.

- Given the selected values of relative photon calorimeter isolation and $p_T^{\mathcal{Q}}$, a value for the relative photon track isolation is sampled.
- Given the selected values of $\Delta\eta(\mathcal{Q},\gamma)$ and $p_T^{\mathcal{Q}}$, a value is sampled for the azimuthal angular separation between $\mathcal{Q}$ and γ, $\Delta\phi(\mathcal{Q},\gamma)$.
- Values for $\eta^{\mathcal{Q}}$ and $\phi^{\mathcal{Q}}$ are sampled from a binned histogram of the corresponding distributions in the data control sample. These are combined with $\Delta\eta(\mathcal{Q},\gamma)$ and $\Delta\phi(\mathcal{Q},\gamma)$ to give the values of η^{γ} and ϕ^{γ}.
- A value for $m_{\mathcal{Q}}$ is sampled from within the required region of $m_{\mu^+\mu^-}$. Separate pdfs are used to describe the $m_{\mu^+\mu^-}$ distributions of resonant $\psi(nS)$ and $\Upsilon(nS)$ production and non-resonant dimuons, which is referred to as "combinatoric" in the following.

The use of this procedure ensures a good description of the background and avoids any reliance on the accuracy or limited sample size of simulated background events.

The nominal selection requirements are imposed and the surviving pseudocandidates are used to construct templates for the $m_{\mathcal{Q}\gamma}$ distributions which are then smoothed using a Gaussian kernel density estimation [67]. Potential contamination of the GR sample from signal events is expected to be negligible, and it was verified, through signal injection tests, that such a potential sig-

nal contamination would not affect the shape of the background model.

The normalisation of the exclusive background from Z FSR is determined directly from the fit to the data. The shape of this background in the $m_{\mu^+\mu^-\gamma}$ distribution is modelled with a Voigtian pdf, while the $m_{\mu^+\mu^-}$ distribution is modelled with a first order polynomial. The parameters of the former pdf are derived from the simulated $Z \rightarrow \mathcal{Q}\gamma$ signal samples. The parameters of the latter pdf are determined directly in the fit to data.

To validate this background model with data, the $m_{\mathcal{Q}\gamma}$ distributions in several regions defined by kinematic and isolation requirements looser than the nominal signal requirements are used to compare the prediction of the background model with the data. Three validation regions are defined using the GR selection as the basis and adding either the $p_T^{\mathcal{Q}}$ requirement (VR1), or the muon isolation requirements (VR2), or the photon isolation requirement (VR3). The $m_{\mathcal{Q}\gamma}$ distributions in these validation regions are shown in Fig. 3 for the $\psi(nS)\gamma$ and the $\Upsilon(nS)\gamma$ final states. The background model is found to describe the data well in all validation regions.

7. Systematic uncertainties

The systematic uncertainties in the expected signal yields are summarised in Table 1. Uncertainties in the Higgs production cross sections are obtained from Ref. [27]. The Z boson production cross section uncertainty is taken from the measurement in Ref. [60].